ADVANCED MATERIALS
www.advmat.de

# Enhanced Reversibility of Iron Metal Anode with a Solid Electrolyte Interphase in Concentrated Chloride Electrolytes

*Min Soo Jung, Sungjin Yang, Cheng Chen, Sathya Narayanan Jagadeesan, Weiyin Chen, Guangxia Feng, Yiming Sui, Ziang Jiang, Emmanuel N. Musa, Nan-Chieh Chiu, Hunter Maclennan, Elliot Holden, Kyriakos C. Stylianou, Ju Li, Chong Fang,* Xueli Zheng,* and Xiulei Ji**

**Iron is a promising candidate for a cost-effective anode for large-scale energy storage systems due to its natural abundance and well-established mass production. Recently, Fe-ion batteries (FeIBs) that use ferrous ions as the charge carrier have emerged as a potential storage solution. The electrolytes in FeIBs are necessarily acidic to render the ferrous ions more anodically stable, allowing a wide operation voltage window. However, the iron anode suffers severe hydrogen evolution reaction with a low Coulombic efficiency (CE) in an acidic environment, shortening the battery cycle life. Herein, a hybrid aqueous electrolyte that forms a solid-electrolyte interphase (SEI) layer on the Fe anode surface is introduced. The electrolyte mainly comprises $FeCl_2$ and $ZnCl_2$ as cosalts, where the Zn-Cl anionic complex species of the concentrated $ZnCl_2$ allows dimethyl carbonate (DMC) to be miscible with the aqueous ferrous electrolyte. SEI derived from DMC's decomposition passivates the iron surface, which leads to an average CE of 98.3% and much-improved cycling stability. This advancement shows the promise of efficient and durable FeIBs.**

## 1. Introduction

Iron, the second most abundant metal element in the Earth's crust (5.6 wt%), is ubiquitous in modern society. It is the most widely used metal in the form of steel alloys and is produced on a tremendous scale, second to no other metals. Iron metal has been used as an anode for rechargeable batteries since the early 1900s, such as the Ni-Fe batteries, where hydroxide ions in alkaline electrolytes serve as the charge carrier to compensate for the charge neutrality of both electrodes. In these batteries, charging converts magnetite ($Fe_3O_4$) to ferrous hydroxide ($Fe(OH)_2$) and subsequently to metallic iron, where the discharge reverses this process.[1] However, albeit with a long lifetime and overcharge tolerance, the Ni-Fe battery suffers from fast self-discharge rates, low efficiency, and the high cost of the nickel-based cathode, making it less competitive than lead-acid batteries.[2] Recently, increasing market demand for grid-scale energy storage systems (ESS) has renewed the interest in iron batteries that employ electrolytes with $Fe^{2+}$ as the charge carrier. These iron batteries, including Fe-redox flow batteries, Fe-$I_2$ batteries, and Fe-ion batteries (FeIBs), operate by iron stripping and plating processes on the anode during discharge and charge, respectively.[3] This mechanism allows a low operation potential of the Fe-metal anode (FeMA) at −0.44 V versus standard hydrogen electrode (SHE), fast reaction kinetics, and potentially a high energy density cell. Furthermore, using an iron metal foil as an anode eliminates the complex manufacturing process necessary for the Fe or $Fe_3O_4$ anode of the Ni-Fe battery, which needs to process powders to form a porous electrode for the best performance.[4]

The primary challenge of the FeMA is its parasitic hydrogen evolution reaction (HER) with aqueous electrolytes, which is a challenge shared by most aqueous metal batteries, including Zn metal batteries.[5] HER compromises the reversibility of the FeMA, which shortens the battery cycle life, limits energy density, triggers premature cell failures, and causes safety concerns. To suppress HER on FeMA, attention has been given to the chemical environment of the electrolyte. Studies on all-iron redox flow batteries revealed that the choice of the anion, pH values of electrolytes, and cosolvents regulating solvation shells can significantly affect the CE of FeMA.[6] Recently, Liu et al. reported a high Coulombic efficiency (CE) of 99.1% for the FeMA in an electrolyte with $MgCl_2$ or $CaCl_2$ as a cosalt and postulated that these

M. S. Jung, S. Yang, C. Chen, Y. Sui, Z. Jiang, E. N. Musa, N.-C. Chiu, H. Maclennan, E. Holden, K. C. Stylianou, C. Fang, X. Ji
Department of Chemistry
Oregon State University
Corvallis, OR 97331, USA
E-mail: chong.fang@oregonstate.edu; david.Ji@oregonstate.edu

S. N. Jagadeesan, G. Feng, X. Zheng
Department of Materials Science and Engineering
Stanford University
Stanford, CA 94305, USA
E-mail: xuelizh8@stanford.edu

S. N. Jagadeesan, G. Feng, X. Zheng
Applied Energy Division
SLAC National Accelerator Laboratory
Menlo Park, CA 94025, USA

W. Chen, J. Li
Department of Nuclear Science and Engineering
Massachusetts Institute of Technology
Cambridge, MA 02139, USA

The ORCID identification number(s) for the author(s) of this article can be found under https://doi.org/10.1002/adma.202419664

**DOI: 10.1002/adma.202419664**

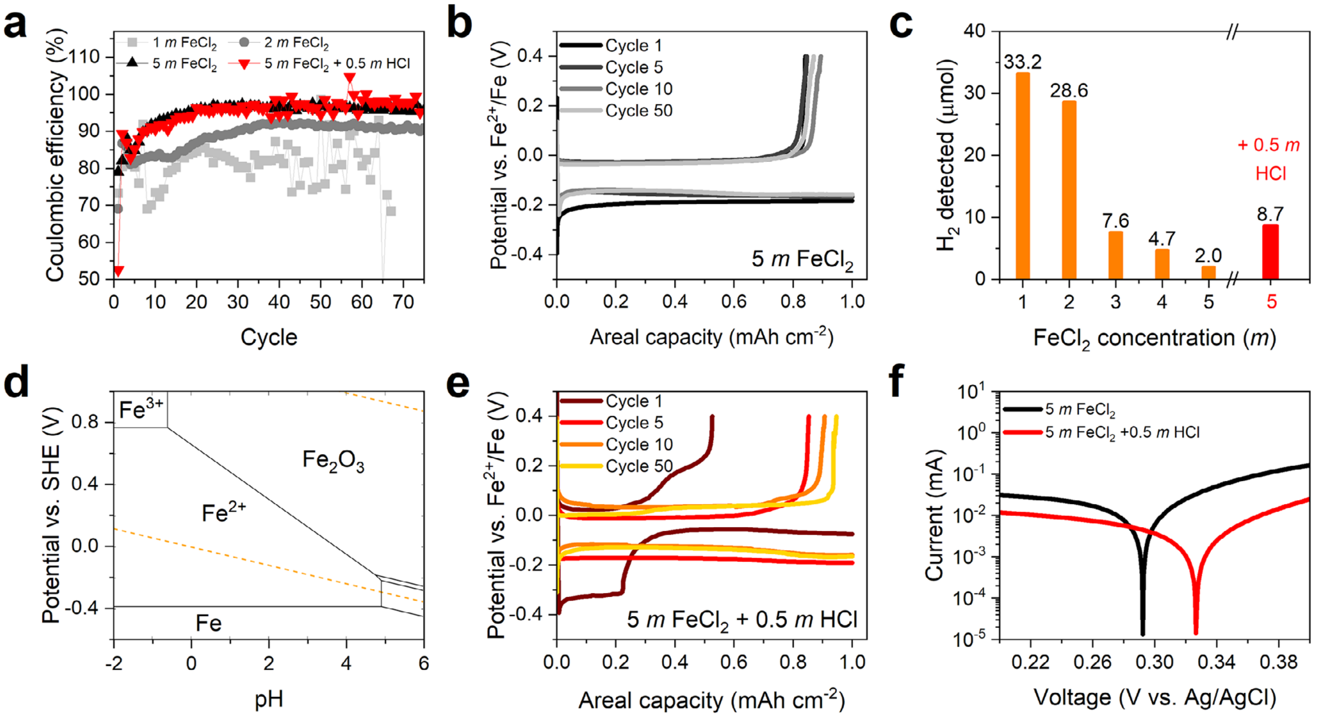

**Figure 1.** The electrochemical performance of FeMA in $FeCl_2$ electrolytes of various concentrations. a) CE of the FeMA measured in three-electrode cells with a Ti foil working electrode and Fe metal foils as both counter and reference electrodes. b) GCD profiles of FeMA in 5 *m* $FeCl_2$. c) The accumulated amount of $H_2$ due to HER after 50 cycles in the headspace of the cells employing various electrolytes. d) Pourbaix diagram of the Fe species simulated for the case where the activity of iron species is 1. e) GCD profiles of the 5 *m* $FeCl_2$ electrolyte with 0.5 *m* HCl added. f) Tafel plots of three-electrode Ti||Fe cell (Ag/AgCl reference) using the 5 *m* $FeCl_2$ electrolyte with and without 0.5 *m* HCl.

cations of high ionic potentials tightly bind water molecules and disrupt the hydrogen bonding network, thus reducing the exposure of water molecules to the surface of FeMA during plating.[7]

In this study, we attempt to give the electrolytes the ability to perform an additional role alongside suppressing the activity of water. Often, the plating of metal anodes is associated with the development of irregular morphologies, commonly referred to as dendrites. This phenomenon is related to the formation of the ion depletion zone and the resulting large electric field near the negatively polarized surface during plating, leading to surface asperities.[8] An approach to tackle the depletion zone is to grow a solid-electrolyte interphase (SEI) layer, wherein the constituent ions are immobilized. More importantly, an SEI layer may passivate metal electrodes, thus rendering them less reactive toward water. However, it is rather difficult for pure aqueous electrolytes to form a passivating SEI because an inorganic SEI often suffers from permeability to water molecules in the electrolytes.

Recently, we reported that a highly concentrated $ZnCl_2$ aqueous solution allows the miscibility of organic solvents, including dimethyl carbonate (DMC), which is widely used in nonaqueous batteries. Our results demonstrated that DMC serves as the precursor for SEI formation on the surface of the Zn metal anode.[9] Although the SEI formation mechanism with DMC is not yet well understood for the Zn metal anode, exploring whether this strategy can also be applied to the FeMA is intriguing. Unfortunately, the common ferrous electrolytes such as $FeCl_2$ or $FeSO_4$ aqueous solutions, regardless of their concentrations, are not miscible with DMC. Herein, we design a hybrid electrolyte solvating both $FeCl_2$ and $ZnCl_2$, where the concentrated $ZnCl_2$ in this electrolyte renders DMC miscible. The addition of DMC results in the formation of an effective SEI that affords stable cycling and a high CE of 98.3% at a current density of 1.0 mA $cm^{-2}$.

## 2. Results and Discussion

We started with 5 *m* $FeCl_2$ as the electrolyte, where the concentration is close to the saturation of 5.4 *m* in $H_2O$ at room temperature. Note that Ti foils were used as a current collector instead of the widely used Cu foil for all the CE tests hereafter. This is to avoid Cu dissolution and galvanic corrosion of iron triggered by leached Cu ions in the highly acidic environment we are testing (Figure S1, Supporting Information). It is also worth mentioning that $Fe^{2+}$ ions in this electrolyte are evidently oxidized when exposed to air, where the electrolyte turned dark orange from yellowish green (Figure S2a, Supporting Information). Therefore, ferrous electrolytes and the FeIB Swagelok cells using them were prepared inside an Ar-filled glove box to minimize air exposure. Our results show that FeMA exhibits an average CE of 94.8% in 5 *m* $FeCl_2$ for 75 cycles at the current density of 1 mA $cm^{-2}$ (a current density employed throughout the study), which is more stable than other low-concentration electrolytes (**Figure 1**a,b). Note that stripping of the plated Fe on the Ti current collector was observed at a potential lower than the Fe reference electrode, which seems erroneous at first glance. In fact, this phenomenon was due to a potential drift of the reference electrode to a higher potential, resulting from the continuous chemical corrosion on the iron surface. While continuous plating and stripping on the working and counter electrodes do not allow an oxide layer to stack on top of these electrodes, the reference electrode without current flow will be clogged with this oxidized species. Galvanostatic charge–discharge (GCD) potential profiles of the counter electrode of iron metal support this explanation, whose stripping also takes place at a potential lower than that of the reference electrode (Figure S3, Supporting Information). Poor CEs of more dilute electrolytes are mainly due to HER, as revealed by the amount of evolved $H_2$ gas in the cell headspace, measured by gas chromatography (GC) after 50 GCD cycles (Figure 1c).

The anodic stability of the $Fe^{2+}$ electrolytes limits the voltage window of the FeIBs, described by the Pourbaix diagram (Figure 1d). Note that the Pourbaix diagram used here is a computed one, assuming that the activity of soluble Fe-ions in the system is unity.[10,11] Under highly acidic conditions, $Fe^{2+}$ is oxidized to $Fe^{3+}$ at 0.77 V versus SHE, which gives FeIBs the thermodynamically widest stability window of 1.21 V. However, under less acidic or neutral conditions, a different reaction pathway triggers $Fe_2O_3$ precipitation at potentials lower than 0.77 V versus SHE, where a unit increase of pH causes a potential drop of 177 mV. However, pure ferrous electrolytes are not sufficiently acidic to prevent $Fe_2O_3$ precipitation. To address this issue, 0.5 *m* HCl is introduced to the 5 *m* $FeCl_2$ electrolyte to ensure sufficient acidity. This amount of HCl was chosen because adding higher concentrations of HCl causes $FeCl_2$ to precipitate as its tetrahydrate.[12] This low-pH $FeCl_2$ electrolyte pushes the onset potential of $Fe^{2+}$ oxidation by ≈30 mV higher at the expense of a CE drop in the first cycle of the GCD cycling test (Figure 1e,f). While the CE recovers to mid-90% a few cycles later, the severe capacity loss in the initial cycles (Figure 1a) is unacceptable in potential practical cells. GC results (Figure 1c) also indicate that the low-pH cells suffer from more HER than pure $FeCl_2$ electrolytes with 3 *m*м or higher concentrations. However, the improved anodic stability of the electrolyte suggests that methods to protect the FeMA under high-acidity electrolytes are worth further investigating.

To mitigate iron corrosion in low-pH $FeCl_2$ electrolytes, we aim to grow an SEI layer on the FeMA using DMC as a cosolvent. However, neither 5 *m* $FeCl_2$ nor its low-pH counterpart forms a miscible solution with DMC, while pure water is somewhat miscible with DMC (Figure S2b–d, Supporting Information). We hypothesized that the hydrated ferrous ions lead to a lesser extent of interactions between water and DMC. Moreover, DMC's partially negatively charged carbonyl oxygen and the $Cl^-$ anions may repel each other. Therefore, we tried adding a cosalt of a different metal chloride that has a standard reduction potential of the cation lower than that of $Fe^{2+}/Fe$ and is potentially to form a chloro complex, such as $[MCl_4]^{2-}$. Formation of such complex ions with a lower charge density may provide a less repulsive environment to DMC and release free water molecules, thus increasing DMC's solubility. Among different metal chlorides, the $ZnCl_2$-added solution exhibits noticeable miscibility, while others show clear phase separation when 10 wt% (vs $H_2O$) of DMC is added to the solution (Figure S2e–i, Supporting Information). Therefore, we added $ZnCl_2$ to the 5 *m* $FeCl_2$ + 0.5 *m* HCl electrolyte to enable the miscibility of DMC with ferrous electrolytes. Adding a small amount of $Zn^{2+}$ species, such as $ZnI_2$, to the $FeCl_2$ electrolyte is known to form Zn-doped iron mass during plating, resulting in smaller Fe particles with enhanced CE.[13] In this study, we added 10 *m* $ZnCl_2$ by considering that a lower concentration of $ZnCl_2$ may not form a sufficient amount of chloride complex as readily and by finding that adding a higher concentration of $ZnCl_2$ leads to ferrous salt precipitation from the hybrid electrolyte. Note that the addition of HCl to the 5 *m* $FeCl_2$ + 10 *m* $ZnCl_2$ is still necessary because it is difficult to achieve the high acidity required after adding $ZnCl_2$. In high concentrations, $Zn^{2+}$ and $Fe^{2+}$ tend to coordinate chloride rather than water, making hydrolysis of water that increases the acidity less likely to happen. The 5 *m* $FeCl_2$ + 10 *m* $ZnCl_2$ electrolyte shows the orange color of ferric ions, and the Ti||Fe cell using it shows an unstable charging profile from the second cycle, which indicates the electrolyte oxidation (Figure S4, Supporting Information). The electrolyte consisting of 5 *m* $FeCl_2$ + 10 *m* $ZnCl_2$ + 0.5 HCl, denoted as FZH electrolyte hereafter, improved the average CE of the FeMA to 95.7% for 75 cycles (**Figure** 2a–c). FZH exhibits lower ionic conductivity than the electrolytes without $ZnCl_2$ but still provides sufficient conductivity for battery applications (Figure S5, Supporting Information). A higher CE may be related to decreased water activity due to its higher overall salt concentration and breakdown of the H-bonding network, which will be discussed with Raman spectroscopy data later. The FZH electrolyte displays an initial plating at a potential of −0.5 V (vs $Fe^{2+}/Fe$ and hereafter), indicating that Zn is coplated with Fe (Figure 2c). On the other hand, the stripping process shows a gradual increase in the stripping potential, which implies that plated Zn and Fe coexist in the same phase. In the following cycles, GCD profiles move up in potential, suggesting the dominance of iron plating and stripping. The fact that the first plating occurs with Zn is attributed to a twice higher concentration of Zn and possibly better affinity of Ti to Zn plating. However, as cycling continues, the electrode surface becomes more favorable to Fe plating as the Fe-containing residues (dead Fe or $FeO_x$) remain on the surface after stripping. Therefore, incorporating $Zn^{2+}$ ions in the electrolyte does not transform a Fe-ion battery into a Zn metal battery. It is worth noting that FZH shows a wider electrolyte stability window compared to 5 *m*м $FeCl_2$ and 5 *m*м $FeCl_2$ + 0.5 *m* HCl (Figure 2e). While cathodic stability only shows a minor deviation, the addition of $ZnCl_2$ significantly enhances the anodic stability by 150 mV. With the improved anodic stability, the FZH electrolyte can deliver a stability window of 1.21 V.

The addition of 10 *m* $ZnCl_2$ transformed the electrolyte's miscibility with DMC, which can dissolve up to 100 wt% of the water in the electrolyte. Adding DMC to the FZH electrolyte increases the average CE of FeMA in general; however, when the DMC amount exceeds 10 wt% versus $H_2O$, it does not show a significant difference (Figure S6, Supporting Information). Hereinafter, the FZH electrolyte with 10 wt% DMC added relative to $H_2O$ is referred to as FZH-DMC. The FZH-DMC performs lower CE than FZH for a couple of initial cycles, which can be attributed to an electrochemical SEI formation (Figure 2a). After these initial low-CE cycles, FZH-DMC continues to show noticeably high CE, starting with 98.6% in the third cycle. Moreover, as shown in Figure S7 (Supporting Information), the cycling stability of the FeMA is greatly improved in FZH-DMC, where more than 150 GCD cycles were demonstrated on the Ti foil current collector with an overall average CE of 98.3%. In comparison, it became unstable before reaching 100 cycles when FZH or 5 *m* $FeCl_2$ + 0.5 *m*

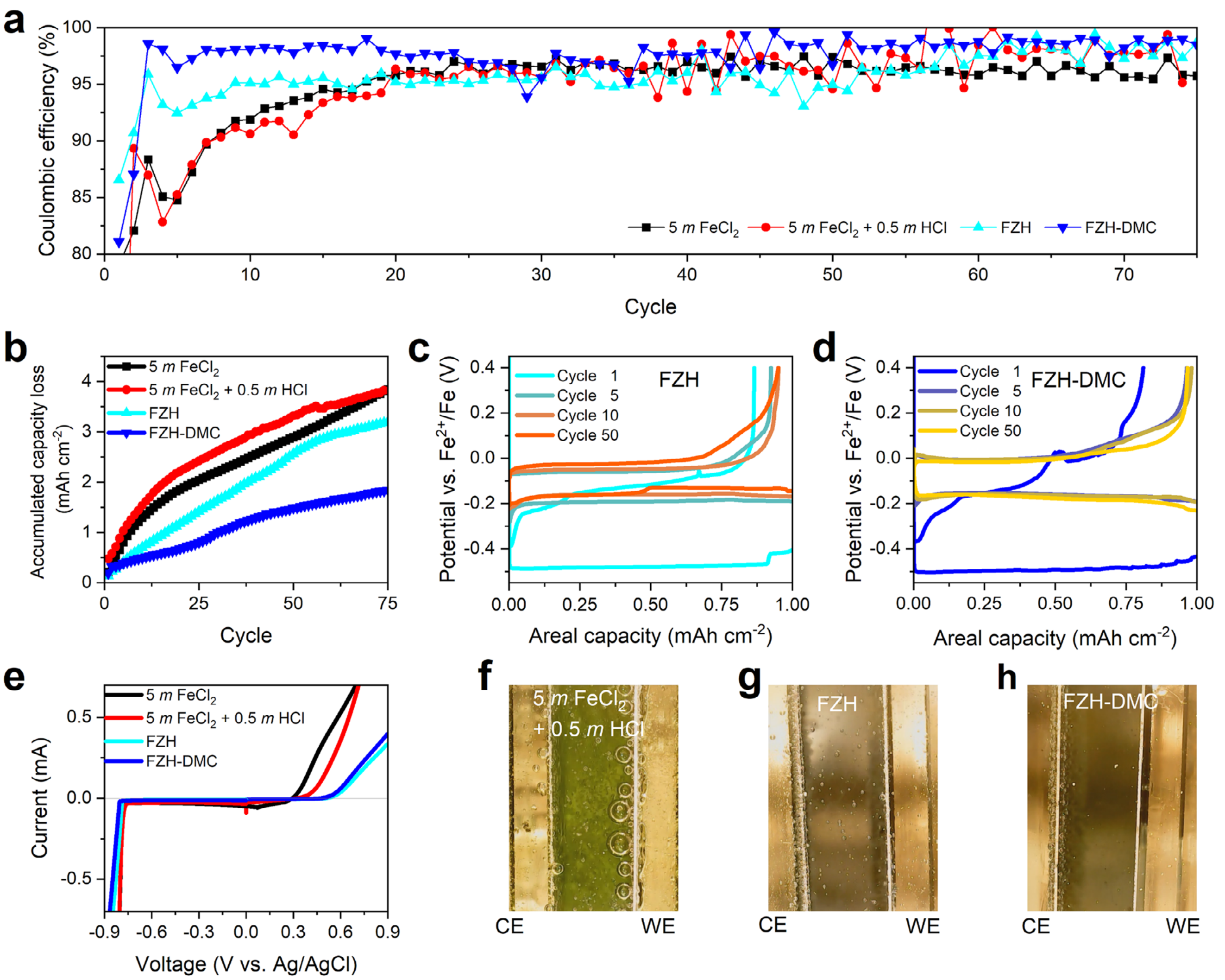

**Figure 2.** Electrochemical results of electrolytes using $ZnCl_2$ as a cosalt. a) CE profiles of the FeMA measured in three-electrode Ti||Fe cells with an Fe reference electrode and b) their accumulated capacity loss of the cells. GCD profiles of c) FZH and d) FZH-DMC electrolytes. e) Stability window of various electrolytes measured by linear sweeping voltammetry (LSV). Snapshot images captured from the videos (Video S1, Supporting Information) recorded using an optical microscope showing gas bubbles generated from the electrode surface, running with f) 5 м $FeCl_2$ + 0.5 *m*м HCl, g) FZH, and h) FZH-DMC as electrolytes.

HCl electrolytes were used. As the cycling continues, SEI continues to develop as each plating process triggers electrochemical SEI formation. The 10-cycle average CE from the 3rd to 12th cycle is 97.9%, while the CE from 141st to 150th cycle is 99.1%. Is SEI just reinforced without any degradation during cycling? We disassembled the cell using FZH-DMC after 10 cycles, reassembled it with different electrolytes, and cycled again (Figure S8a, Supporting Information). Interestingly, these reassembled DMC-free cells show CE values close to their refilled electrolytes rather than the improved value of FZH-DMC. This indicates that SEI is damaged in the DMC-free environment, possibly when all the Fe mass is stripped out during the stripping process. If continuous degradation and reformation of SEI happen in every cycle, it possibly results in a thickened SEI as the cycle number increases. Indeed, a larger overpotential is observed in the later cycles of the FZH-DMC cells, especially at the beginning of a plating process due to the nucleation overpotential. After the 180th cycle, the plating process starts with a potential around −0.4 V versus $Fe^{2+}/Fe$, where Zn plating is viable (Figure S8b, Supporting Information). This low-potential plating does not last for a long time; however, it causes large fluctuations in the CE values. Moreover, after the 190th cycle, the galvanostatic cycling became extremely unstable. For example, sudden spikes appear in the potential profile during the plating process, which can be attributed to the micro short-circuit, and the potential profiles at the end of the stripping became noisy, leading to the measured CE being over 100% (Figure S8c, Supporting Information). This indicates that the severe degradation of SEI in the later cycles can be detrimental to the cycling performance.

GC analysis of the gases collected from the headspace of the cycled cells confirmed that the improved electrochemical performance of the FZH-DMC arises from HER suppression (Table S1,

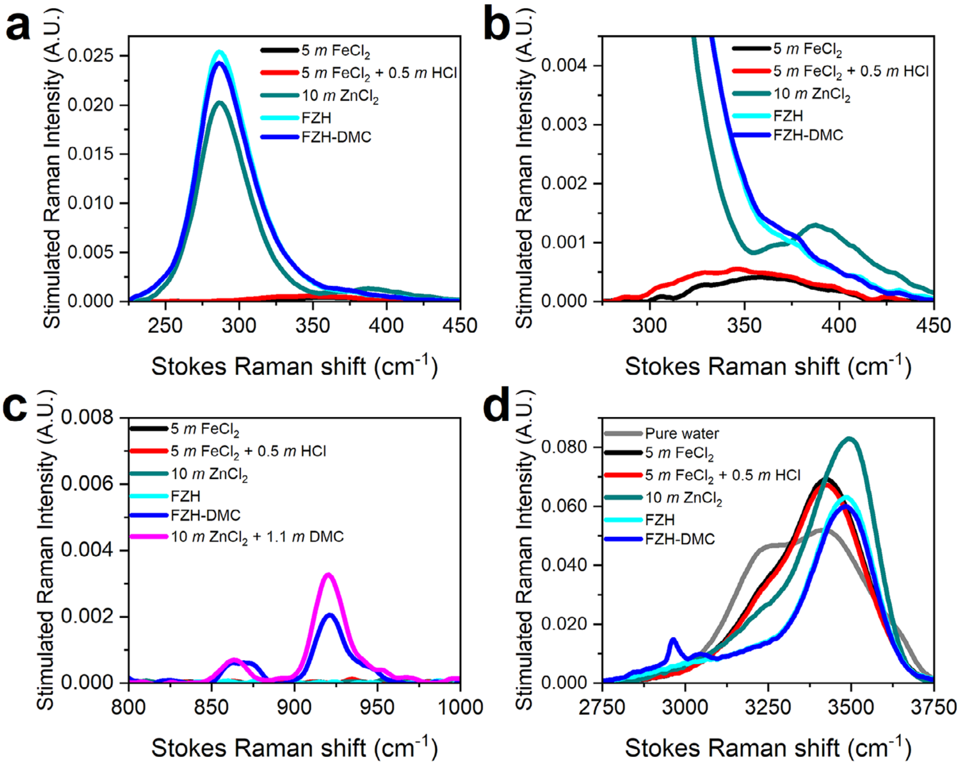

**Figure 3.** Ground-state FSRS spectra of various electrolytes in the a) low-frequency region showing ion clusters. b) Enlarged view of the hydrated cluster region. c) Mid-frequency region depicting water–DMC interactions, and d) high-frequency region of the H-bonding network of water.

Supporting Information). After 50 cycles of plating and stripping at 1 mA cm$^{-2}$ with a capacity of 1 mAh cm$^{-2}$, the amount of hydrogen gas accumulated inside the cell using FZH-DMC as the electrolyte is less than 20% compared to the cell using the FZH electrolyte. The images and videos collected from in situ optical microscopy studies on transparent cells reveal the different extents of HER in these electrolytes (Figure 2f–h), where the FZH-DMC electrolyte delivers a more tranquil process in contrast to the "stormy" bubbling scenes in other electrolytes. Intriguingly, the Fe working electrode of the cell comprising the FZH-DMC electrolyte generates fewer bubbles than the counter electrode in the same cell. Such a disparity was not observed in the cells hosting other electrolytes. This difference between two electrodes in the same cell suggests different surface properties acquired by the iron metal electrodes after an initial voltage bias was applied. Notably, the working electrode experienced a plating process, while the counter electrode underwent a stripping process when the video was taken. The fact that an anodic process shows a more immense amount of hydrogen bubbles than a cathodic process is somewhat counterintuitive from an electrochemical perspective. Electrochemically, hydrogen evolution is accelerated when the potential applied to the electrode decreases. However, in this case, stripping the iron electrode by applying a higher potential shows more extensive hydrogen gas evolution. Therefore, it can be reasonably deduced that the electrochemical plating and stripping processes of the Fe electrodes cause a drastic difference in surface properties that determine HER kinetics, which affect both electrochemical and chemical reaction pathways. Specifically, an SEI formed during the plating process can passivate the surface during the plating process, while the stripping exposes more reactive fresh Fe sites. To test this, Fe foils were immersed in different electrolytes, and the amount of $H_2$ gas accumulated inside the vial was measured using GC (Table S2, Supporting Information). The Fe foil immersed in the FZH-DMC electrolyte for 100 h only showed a 10% decrease in the amount of $H_2$ gas compared to the FZH electrolyte. Compared to the dramatic decrease of $H_2$ gas detected in the cycled cells, this result indicates that the major effect of the DMC addition is driven by electrochemical reactions, although the dilution of the electrolyte by DMC also slightly suppresses the activity of water. It is also worth noting that the 5 *m* $FeCl_2$ + 0.5 *m* HCl electrolyte shows more than ten times $H_2$ gas contents compared to FZH in the Fe foil immersion test. This implies that the addition of 10 $ZnCl_2$ suppresses the reactivity of water dramatically. Also, considering the large amount of electrolyte used in the immersion test (2 mL) compared to the electrolyte conditions (0.1 mL) used in the air-tight Swagelok cells for GC tests after cycling, this result demonstrates that drying out of the electrolyte due to HER has unignorable impact to the practical lean electrolyte cells.

The electrochemical properties of electrolytes closely pertain to the chemical environment of the electrolytes, which were investigated using the femtosecond stimulated Raman spectroscopy (FSRS) technique in the electronic ground state at equilibrium. In a low-frequency region (**Figure 3**a,b), 5 *m* $FeCl_2$ and its acidic counterpart exhibit a weak broad peak around 360 and 350 cm$^{-1}$, respectively, which can be assigned to the hydrate complex of ferrous ions with octahedral coordination. The redshifted peaks compared to the literature values, i.e., 390 cm$^{-1}$, can be attributed to the concentrated electrolytes where ferrous ions are exposed to a more chloride-rich environment.[14] It is known that some of the water molecules can be replaced by chloride ions in high concentrations, forming $[Fe(OH_2)_{6-x}Cl_x]^{2-x}$ complex ions.[15] These partially chloride-substituted species are also expected to be Raman-active (see the Supporting Information for details, Tables S3–S5, Supporting Information).[16] The detailed compositions of the coordinated ions will be discussed in a later section, along with the synchrotron XAS results. On the other hand, the 10 *m* $ZnCl_2$ solution has two pronounced peaks in the same region. While the small peak around 390 $cm^{-1}$ is assigned to the hexahydrate complex of zinc ions, a large peak at a lower frequency around 290 $cm^{-1}$ is attributed to tetrachlorozincate complex ions ($[ZnCl_4]^{2-}$).[17] Interestingly, this Zn-Cl complex peak exhibits a stronger intensity in the FZH electrolyte (Figure 3a), which can be attributed to the formation of more $[ZnCl_4]^{2-}$ ions due to the additional chloride ions from 5 *m* $FeCl_2$ and 0.5 *m* HCl. Accordingly, the $[Zn(OH_2)_6]^{2+}$ Raman peak around 390 $cm^{-1}$ displays a notable intensity drop (Figure 3b) because fewer $Zn^{2+}$ ions are hydrated due to their preferable coordination with extra chloride ions. These spectral results do not negate the notion that more chlorinated $[Fe(OH_2)_{6-x}Cl_x]^{2-x}$ ions are possibly formed after 10 *m* $ZnCl_2$ is added to the 5 *m* $FeCl_2$, considering the seemingly broadened peak at ≈290 $cm^{-1}$ (more broadened on the higher-frequency side) of the electrolytes comprising both $FeCl_2$ and $ZnCl_2$ versus that of 10 *m* $ZnCl_2$.

The addition of DMC to the FZH decreases the intensity of major peaks shown in the FZH electrolyte, such as the $[ZnCl_4]^{2-}$ peak around 290 $cm^{-1}$ and DA mode of water around 3490 $cm^{-1}$ (Figure S9, Supporting Information). These decreased peaks show no changes in the frequency, which demonstrates the diluting effect of DMC. Figure 3c shows new peaks that arise around 860 and 920 $cm^{-1}$, which can be assigned to the O—C—O stretching modes of DMC split into two peaks due to their interactions with water molecules.[9] These results support our hypothesis that DMC primarily interacts with water molecules, and the presence of soft $[ZnCl_4]^{2-}$ anions helps dissolve DMC.

Figure 3d shows the Raman spectra in the high-frequency regions that depict changes in the H-bonding network of water across various electrolytes. Compared to pure water, the 5 m $FeCl_2$ electrolyte shows a decrease in the double donor–double acceptor configuration (DDAA, 3245 $cm^{-1}$) and an increase in the donor–acceptor configuration (DA, 3420 $cm^{-1}$), attributed to $Fe^{2+}$ hydration.[18] In the more concentrated FZH and FZH-DMC electrolytes, the DDAA mode nearly vanishes, and the DA mode blueshifts to higher energy (3490 $cm^{-1}$) with a decreased intensity versus 5 m $FeCl_2$. The diminished DDAA mode suggests that the bulk H-bonding network is severely disrupted because of the highly concentrated hydrated ions with $Fe^{2+}$ or $Zn^{2+}$ ion centers. Furthermore, the blueshift of the DA mode peak indicates stronger O—H bonds of water for that water configuration, which may help suppress HER.[19]

X-ray absorption spectroscopy (XAS) measurements were carried out to further investigate the solvation structures of the ferrous ionic species in the concentrated chloride electrolytes. Different local environments of $Fe^{2+}$ cations in concentrated chloride electrolytes resulted in the change in the Fe K-edge X-ray absorption near edge structure (XANES) and the extended X-ray absorption fine structure (EXAFS) features (**Figure** 4a,b). The change in solvation structures is indicated by the high-energy shifted absorption energy of Fe K-edge at the half-edge step, ½ $\mu$(E), in concentrated chloride electrolytes of +0.6 eV with the addition of 10 m $ZnCl_2$ (FZH) and +0.7 eV with 10 *m*M $ZnCl_2$ and 1.1 *m* DMC added (FZH-DMC). Further evaluation was conducted by $f_{eff}$ fitting of the EXAFS spectra.[20] As shown in Figure 4b–d, the EXAFS spectra were fitted well in the *k* range of 0–10 $Å^{-1}$, with an R range of 0.5–5 Å. In all electrolytes, O and Cl atoms were identified as the close neighbors in the first coordination shell (Figure S10, Supporting Information). Structural parameters of the local environments of the $Fe^{2+}$ cations in the aqueous electrolytes, such as the average number of neighbor atoms (N), distance (R), and Debye–Waller factor ($\sigma^2$), are listed in Table S6 (Supporting Information). The amplitude reduction factor and the shift of energy origin were fixed at $S_0{}^2 = 0.6 \pm 0.1$ and $\Delta E_0 = -8.2 \pm 0.2$ eV, respectively. $f_{eff}$ fitting results indicate that two of the water molecules are replaced by chlorides in 5 *m*M $FeCl_2$ and 5 *m* $FeCl_2$ + 0.5 *m* HCl electrolytes, forming $[Fe(OH_2)_4Cl_2]$.[15,21] Intriguingly, this composition is the same as the hydrated solid of ferrous chloride we used to prepare electrolytes in this study. As the chloride concentration increased in the FZH and FZH-DMC electrolytes, one of the O neighboring atoms coordinated with $Fe^{2+}$ in the first solvation shell was replaced by a Cl atom with an increased interatomic distance, R. An increased electron density is observed from this newly formed Fe-Cl coordination corroborated with the positive ½ $\mu(E)$ energy shift of Fe K-edge in concentrated chloride electrolytes. Moreover, the higher values of Debye–Waller factors for the Fe—Cl bond indicate a more significant static disorder of Cl atoms surrounding the $Fe^{2+}$ cations. This implies that the asymmetric broadening of FSRS peak at 290 $cm^{-1}$ observed in FZH and FZHDMC (Figure 3a,b) is due to the formation of $[Fe(OH_2)_3Cl_3]^-$ instead of $[Fe(OH_2)_4Cl_2]$, where weaker interactions between the ferrous ion and chloride ions makes the peak redshifted from 350 $cm^{-1}$ of 5 *m* $FeCl_2$ + 0.5 *m*M HCl.

The FeMA plated from different electrolytes was characterized by field emission scanning electron microscopy (FE-SEM) imaging and energy dispersive X-ray spectroscopy (EDS) elemental mappings (**Figures** 5a–d, and S11, Supporting Information). In the 5 *m* $FeCl_2$ electrolyte, discrete iron particles of several micrometers in size were sparsely plated, where the surface of the Ti current collector was not fully covered. Turning 5 *m* $FeCl_2$ more acidic by adding 0.5 *m* HCl reduced the particle size to 1–2 µm and gave rise to a higher coverage on the Ti surface. In sharp contrast, the conformal film consisting of more granular particles nearly covered the entire Ti surface in the electrode using FZH electrolyte, albeit with cracks. Larger particles of several micrometers in size are deposited on top of this conformal film. The results are consistent with a previous study introducing $Zn^{2+}$ in the Fe electrolyte.[13] Iron plated in the FZH-DMC electrolyte shows a similar morphology of a conformal film without any noticeable cracks, which coats the Ti surface more uniformly than the FZH electrolyte. These intriguing results, which show that iron is plated differently depending on the electrolytes, can be explained by differences in the solvation structures of ferrous ions. Ferrous ions in 5 *m* $FeCl_2$ and 5 *m* $FeCl_2$ + 0.5 *m*M HCl are mainly solvated by two chlorides and four water molecules, making the entire complex charge neutral. $[Fe(OH_2)_4Cl_2]^0$ would favor being reduced on the top of the plated iron mass, as it provides

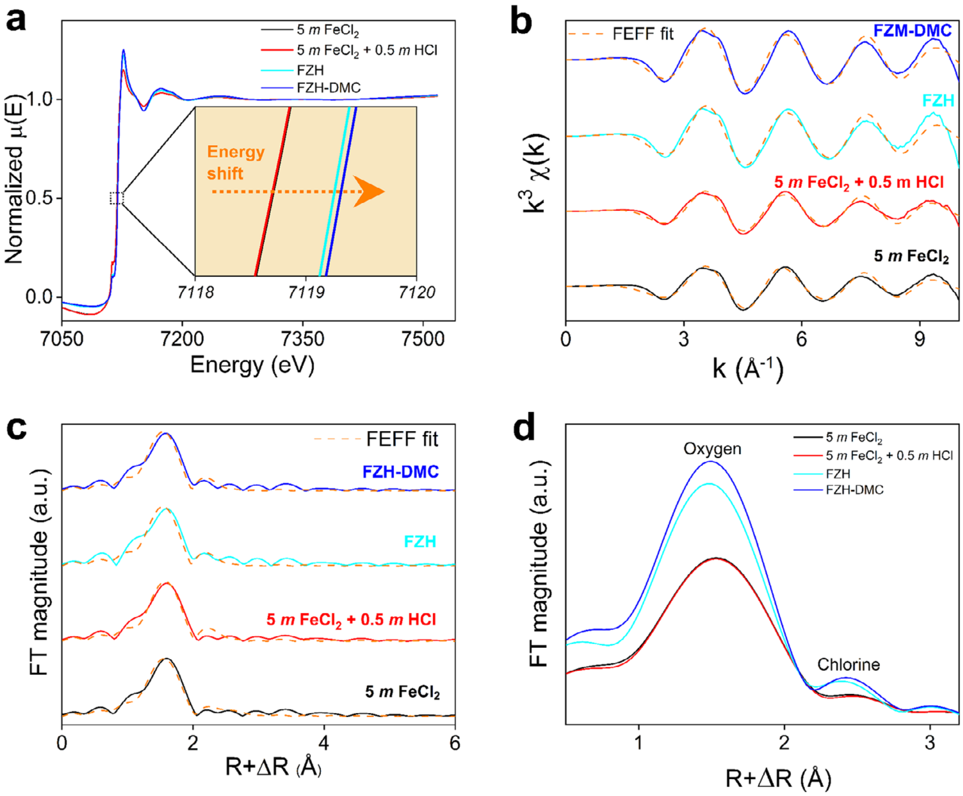

**Figure 4.** XAS measurements using synchrotron light source. a) Normalized Fe K-edge XANES with an inset of the energy shift at ½ $\mu(E)$ in concentrated chlorine electrolytes. b) The $k^3$-weighted Fe K-edge EXAFS spectra, and c) their corresponding Fourier Transform (FT) magnitude of the electrolytes (solid line – experimental results, orange dashed line – best $f_{eff}$ fits of the EXAFS model in the R range of 0.5–5 Å). d) FT magnitude of the electrolytes overlapped.

a shorter diffusion length. However, in FZH and FZH-DMC electrolytes, where the higher chloride concentration leads to one more chloride participating in the solvation structure, forming the negatively charged $[Fe(OH_2)_3Cl_3]^-$. This anionic complex ion can be affected by the electric field developed around the deposited mass. The protruding metal asperities create a stronger electric field along the convex tips (Figure 5e).[22] Therefore, $[Fe(OH_2)_3Cl_3]^-$ approaching the plating electrode tends to avoid this strong electric field zone around the existing nuclei and ends up nucleating on the Ti surface next to it. This is also the same for zinc ions in the FZH and FZH-DMC, as the dominant coordination of zinc ions in these electrolytes is $[ZnCl_4]^{2-}$. Besides, Zn mapping data and quantitative elemental analysis of SEM-EDS showed that Zn is also evenly distributed across the surface of plated mass (Figure S12 and Table S7, Supporting Information). It is also noteworthy that the plated iron surface had an increased amount of carbon elements when FZH-DMC was used, which indicates the SEI formation during the plating process.

To understand the role of the $Zn^{2+}$ during plating, we collected X-ray diffraction (XRD) patterns of the working electrodes after the 50th plating (Figure 5f). From 5 $FeCl_2$ and 5 *m* $FeCl_2$ + 0.5 *m*м HCl, the plated iron mass exhibits the cubic *α* phase, having a lattice constant of 2.87 Å and coherence lengths of 36.2 nm (5 *m* $FeCl_2$) and 33.7 nm (5 *m* $FeCl_2$+0.5 *m* HCl), calculated using the Williamson–Hall method.[23] However, from FZH and FZH-DMC, the plated mass has lattice constants of 2.88 and 2.89 Å, respectively. This lattice expansion implies that small amounts of Zn are also plated alongside Fe when $ZnCl_2$ is present in the electrolyte, forming a Zn-doped *α*-Fe lattice. Judging by the extent of lattice expansions, it is estimated that Zn constitutes ≈7 and ≈12 at% in the plated file from FZH and FZH-DMC, respectively.[24] The coherence lengths of the plated metallic mass are also drastically shortened to 1.34 nm (FZH) and 2.4 nm (FZH-DMC), which also support our hypothesis that strong electric fields on the tips of nuclei repel the negatively charged complex anions of these electrolytes, inhibiting the further growth of existing nuclei.

X-ray photoelectron spectroscopy (XPS) was used to further evaluate the SEI formation on the deposited metal mass. We analyzed the working electrode after the 50th discharge to make sure the SEI layer formed is matured enough with a certain thickness that the depth profiling can show the difference. The 50th cycle reaches the point where the trend of CE is stabilized; the average CE (10 cycles moving average) continuously shows a value higher than 98% (Figure S7b, Supporting Information). After the 50th plating, the electrode using FZH-DMC shows a stronger C═O signal (532 eV) in the O 1s spectrum than electrodes cycled in other electrolytes, which again suggests the presence of DMC-derived SEI (**Figure 6a**).[25] Figure 6b shows the Fe 2p spectra, where the peak at 711 eV is generally attributed to $Fe_2O_3$, and the peak at 706 eV can be assigned to the metallic iron.[26] The depth profiles obtained by Ar sputtering inform the extent of surface corrosion. In 5 *m* $FeCl_2$ and 5 *m* $FeCl_2$ + 0.5 *m* HCl, the $Fe_2O_3$ peak remains strong until 20 and 100 nm depth of sputtering, respectively. However, in FZH and FZH-DMC, the $Fe_2O_3$

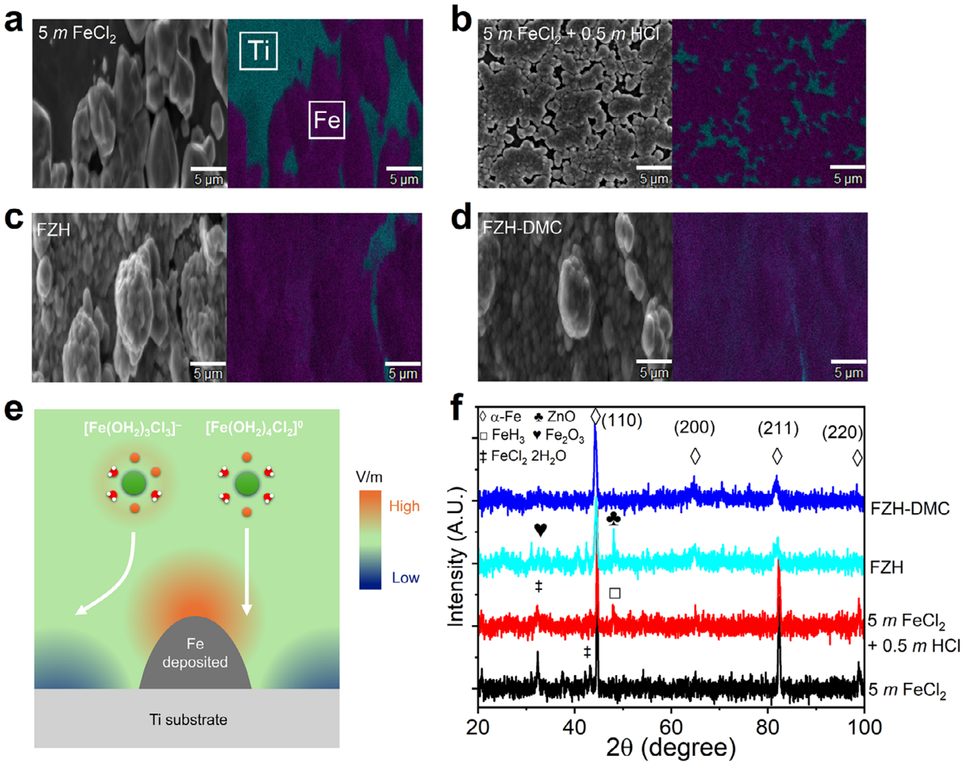

**Figure 5.** SEM images of the plated mass on a Ti current collector, taken after the 10th discharge using electrolytes of a) 5 *m* $FeCl_2$, b) 5 *m* $FeCl_2$ + 0.5 *m* HCl, c) FZH, and d) FZH-DMC. e) Schematic illustration of the electric field distribution around the deposited iron mass and its effect on the ferrous ions with different solvation structures. f) XRD patterns of the electrodes after the 50th discharge using various electrolytes.

peak disappears after 20 nm of sputtering, indicating a lesser extent of iron corrosion. Notably, without sputtering, the metallic iron peak is evident when using FZH-DMC, demonstrating the protective role of DMC for the electrode surface. Moreover, the peak assigned to the oxidized iron species across different spectra shifts to a lower binding energy as sputtering continues, which indicates the progressively increasing and decreasing presence of $Fe^{2+}$ and $Fe^{3+}$ species, respectively, when approaching the metallic iron surface.[27]

The Zn $2p_{3/2}$ depth-profiling XPS results support the incorporation of Zn into deposited Fe during plating (Figure 6c), as indicated by XRD (Figure 5f). As the sputtering exposes deeper layers of atoms, the binding energy of Zn $2p_{3/2}$ redshifts, suggesting a transition from the Zn-ion-rich SEI layer to the metallic Zn underneath.[28] In the C 1s spectra of the electrodes, all the electrodes exhibit an O—C═O peak at 289 eV, which does not negate the decomposition of DMC to form a carbonate-containing surface film (Figure 6d,e; and Figure S13, Supporting Information).

Furthermore, we employed galvano electrochemical impedance spectroscopy (GEIS) to study the transport properties on the FeMA surface during the first plating and stripping cycle. The distribution of relaxation times (DRT) calculated from each set of the acquired GEIS is plotted with the cell's voltage profiles (**Figure** 7). Compared to FZH, FZH-DMC displays higher resistance for the time constant peaks around $10^{-3}$ s for the first plating process and around $10^{-2}$ s for the first stripping. These time constant peaks can be assigned to ion transports through the interphase of electrodes. The higher resistance with DMC in the electrolyte corroborates the SEI formation at an early stage of plating, thus corroborating the results of the optical microscopy (Figure 2g,h). Note that the first plating for both electrolytes occurs at Zn-plating potentials. Notably, the peak shifts to a higher time constant upon stripping, suggesting that Fe stripping is more sluggish than Zn plating.

In the following cycles, the plating process starts with a dominant peak of a similar time constant with the stripping process, indicating major Fe deposition (Figure S14, Supporting Information). The interesting point is that it shows a decrease in the time constant in the later phase of the plating process. This might indicate the activation energy of nucleation has decreased, possibly because the reaction changes from Fe deposition on the Ti surface to Fe deposition on the Fe surface. This explanation can be supported by the morphology of the plated mass observed with SEM, which shows the conformal Fe film and Fe particles on top of the film (Figure 5c,d). When the conformal film formation is over, or all the surface is covered with Fe, then the only option left is Fe deposition on the Fe surface.

Finally, we evaluated whether FZH-DMC can be used in a FeIB full cell with active cathode materials on board. $VO_2$ is chosen as a model cathode as its $V^{4+}/V^{3+}$ redox couple is expected to have a moderate operating voltage that does not oxidize ferrous ions in the electrolyte. **Figure** 8a shows the XRD pattern of $VO_2$ synthesized following the literature, with major peaks matching well with the reference data (PDF#01-081-2392).[29] Figure 8b,c displays representative GCD profiles and cycling performance of the $VO_2$|FZH-DMC|Fe cell at a current rate of 50 mA $g^{-1}$. A

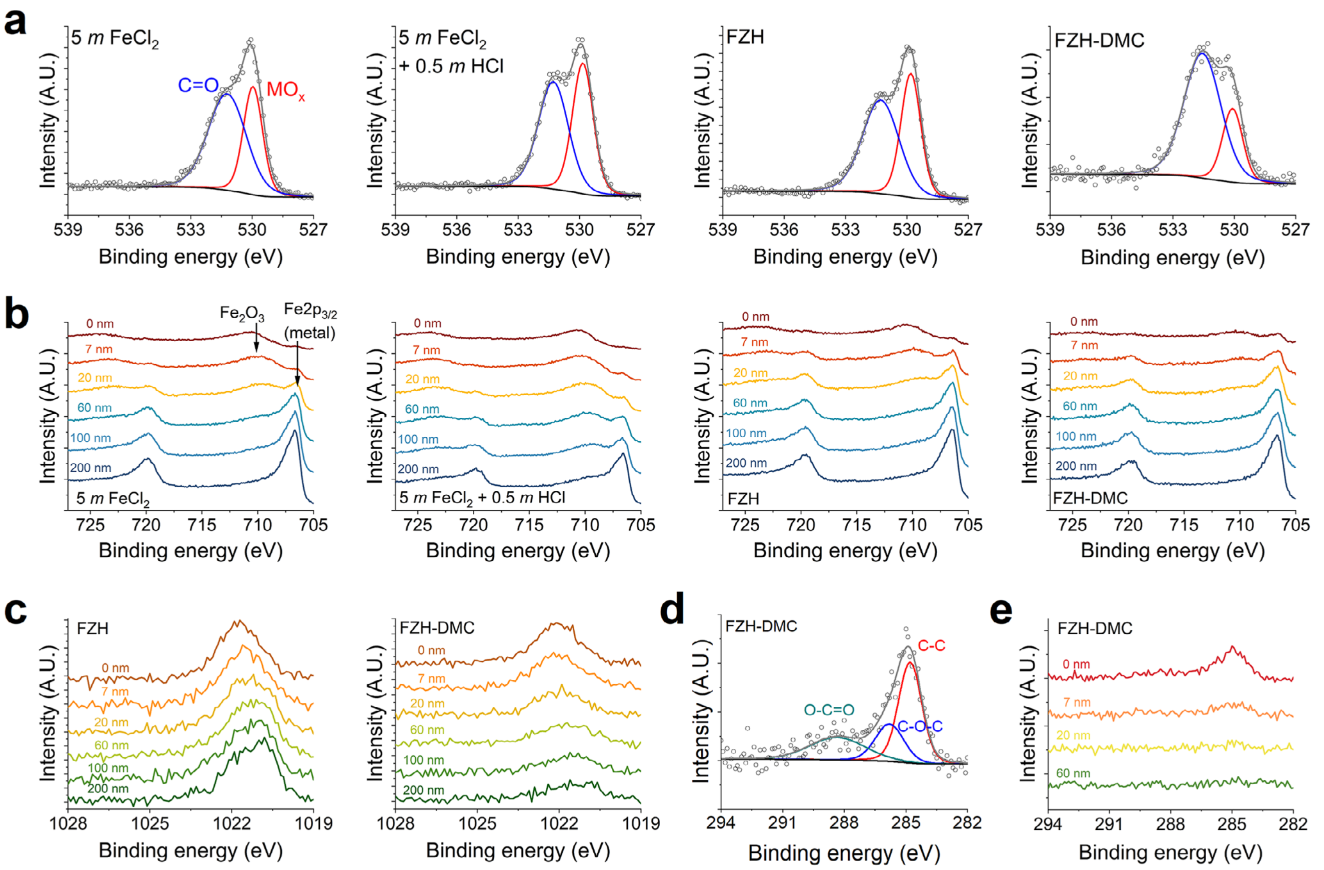

**Figure 6.** XPS profiles of anode after 50th discharge with various electrolytes. a) Peak deconvolution results of the O 1s spectra. Depth profiling of b) Fe 2p and c) Zn 2p spectra. d) Peak deconvolution results of the C 1s spectra and e) depth profiling of the C 1s spectra for FZH-DMC samples.

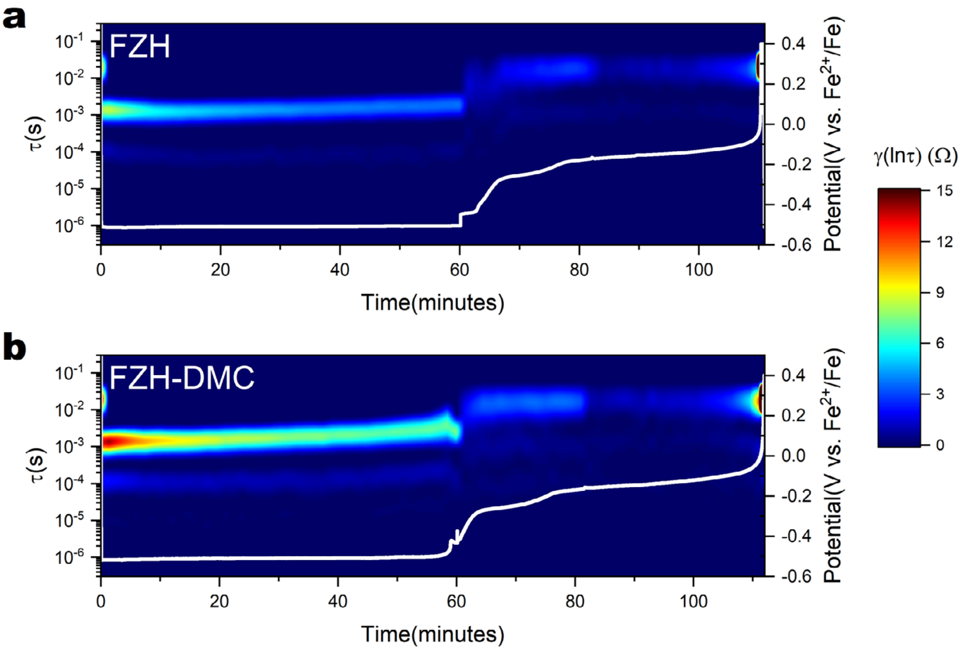

**Figure 7.** GEIS-DRT data of the first cycle of the plating and stripping on the Ti current collector using electrolytes of a) FZH and b) FZH-DMC.

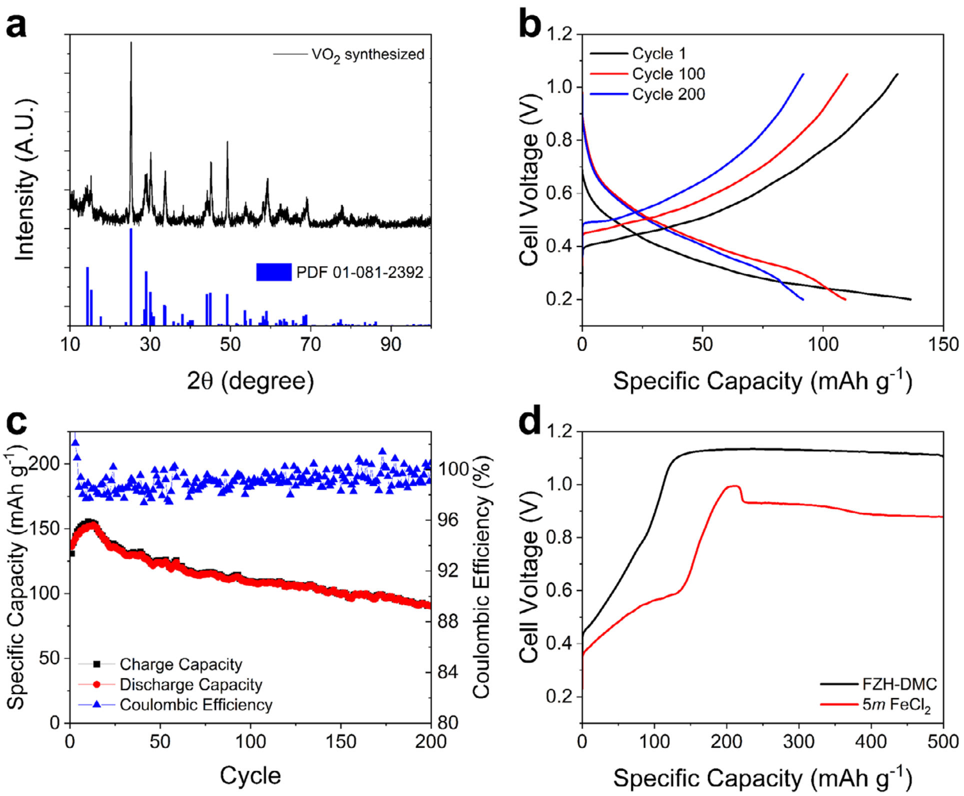

**Figure 8.** Electrochemical data of FeIBs utilizing VO$_2$ as a model cathode. a) XRD pattern of VO$_2$ synthesized and the corresponding ICDD card PDF#01-081-2392. b) Representative GCD profiles of the VO$_2$|| Fe cell and c) its cycling performance. d) Unlimited galvanostatic charging profiles of VO$_2$||Fe cells using different electrolytes.

cell potential range of 0.2–1.05 V was used to limit the Fe$^{2+}$ oxidation on the cathode surface. It delivered a specific capacity of 152 mAh g$^{-1}$ and capacity retention of 60% after 200 cycles, with the average CE near 99% and the round-trip energy efficiency of 65%. Compared to the widely used lead-acid battery, which shows about 80% energy efficiency, more work should be done on FeIBs for practical use.[30] Finding a suitable cathode material that gives high capacity, better capacity retention, and does not oxidize the electrolyte is a pressing need for FeIBs. Figure 8d shows GCD profiles of the VO$_2$||Fe cell using 5 *m* FeCl$_2$ and FZH-DMC electrolytes with an increased cutoff voltage for the charging step. Compared to the 5 *m* FeCl$_2$ electrolyte, which exhibits an "endless" charging plateau at a cell potential around 0.9 V, FZH-DMC shows no ferrous ion oxidation until 1.1 V is reached. The results are consistent with the electrolyte voltage window tests using LSV (Figure 2e).

## 3. Conclusions

In this study, we investigated the electrochemical performance of Fe metal anodes in FeCl$_2$-containing hybrid electrolytes. Introducing 0.5 *m* HCl to the 5 m FeCl$_2$ electrolyte mitigates Fe$_2$O$_3$ precipitation; however, the acid addition promotes HER. Therefore, we explored the SEI formation using DMC as a cosolvent whose miscibility is mediated by the high-concentration ZnCl$_2$ as a cosalt. This hybrid electrolyte demonstrates great promise in improving the electrochemical performance with a high Coulombic efficiency and enhanced cycling stability of Fe metal anode. Our characterization results support that SEI is formed on the iron metal anode in this hybrid electrolyte. The study highlights the potential of FeCl$_2$-based electrolytes (with the right ingredients) to enhance the performance of Fe metal anodes. Future work should focus on optimizing the electrolyte composition and exploring alternative additives to further improve the stability and efficiency of Fe-ion batteries.

## 4. Experimental Section

*Materials Preparation*: Zinc chloride (ZnCl$_2$, anhydrous, ≥98%, Alfa Aesar) was used without further processing. Iron(II) chloride tetrahydrate (FeCl$_2$·4H$_2$O, ≥99%, Sigma-Aldrich) was immediately transferred inside the Ar-filled glove box as received to prevent oxidation. Water (HPLC grade, Sigma-Aldrich), hydrochloric acid solution (37 wt%, Sigma-Aldrich, diluted to 7.4 wt% with HPLC grade water), and dimethyl carbonate (anhydrous, ≥99%, Sigma-Aldrich) were purged with argon gas for 2 h using a FlowPrep 060 gas purging system (Micromeritics) to remove dissolved oxygen before being transferred into the Ar-filled glove box. All the electrolytes were made (including heating and stirring) and kept inside the Ar-filled glove box. Iron foil (soft ingot iron, 99.8%, 0.5 mm thickness, Goodfellow) was punched into a 7/16-in. diameter. Iron disks punched out were usually deformed to cone-shape by the punch press, and they were pressed with a hydraulic press to be flat. The flattened disks were rinsed with acetone (≥99.5%, Fisher chemicals) and stored inside the glove box. Titanium foil (0.01 mm thickness, Shaanxi Titanium Aviation New Material Technology) was first rinsed with acetone and soaked in concentrated nitric acid (70 wt%, Fisher chemicals) to remove surface contaminants, then cut to

12 mm disks and transferred into the Ar-filled glove box. $VO_2$ cathodes were prepared using a hydrothermal reaction similar to the literature.[29] Polytetrafluoroethylene (PTFE) liner of the hydrothermal reactor (45 mL in internal volume) was filled with 8 mL of ethylene glycol and 12 mL of deionized water. $V_2O_5$ powder, 2 g, was added to this solution and vigorously stirred for an hour. Then, the reactor is sealed, transferred to the oven, heated up to 160 °C, and kept for 6 h. The heating rate was regulated to be 5 °C $min^{-1}$. After cooling down to room temperature, dark blue powders were collected from the reactor and rinsed with acetone. The remaining powders were dried in the oven at 80 °C for 12 h. To fabricate an electrode, $VO_2$, KetjenBlack (EC-600JD), and polyvinylidene fluoride (PVdF) binder are mixed in a 7:2:1 ratio using N-Methyl-2-Pyrrolidone (NMP) as a solvent. The slurry made was coated on Ti foil and dried at 100 °C to remove the solvent. An average active mass loading of 1.5 mg $cm^{-2}$ was used.

*Electrochemical Characterization*: Galvanostatic cycling tests of plating and stripping iron on the Ti foil were conducted using three-electrode Swagelok cells, using a Fe disk as a counter electrode and a separate Fe disk as a reference electrode. Glass fiber filter papers (GF/F grade, Tisch) were used as separators and 0.1 mL of the electrolytes were used for each cell. Cells were kept inside the Ar-filled glove box during the cycling and connected to the battery cycler (CT3002A, Landt) using cables through the service ports of the glove box. The current density used was 1.0 mA $cm^{-2}$ against the working electrode (12 mm Ti foil disk). The plating capacity was 1.0 mAh $cm^{-2}$, and the stripping cutoff potential was 0.4 V versus the reference electrode. LSV was performed using the same setup with some modifications; the reference electrodes were changed to the Ag/AgCl (3 м KCl), and the battery cycler was changed to the potentiostat (VMP-3, Biologic). The scan rate for all the experiments was 1 mV $s^{-1}$.

*Transparent Cell Tests*: A homemade transparent cell was used to record the optical images of the cell during operation. The quartz cuvette cell (LAB4US, 2 mm thickness) was used to fix the iron electrodes. There was no separator inside the transparent cells, and the gap between the two iron foils was ≈2.5 mm. The area of the iron foil immersed inside the electrolyte was ≈3 $cm^2$. The current density used for all the experiments was 1.0 mA $cm^{-2}$ for the charging and discharging processes. The temperature was maintained at ≈45 °C.

*Ex Situ GC after Cycling*: Custom cells using airtight Swagelok PFA tube fitting were used to trap $H_2$ evolved inside the cell headspace. The detailed design can be found in the previous publication.[31] Headspace gas samples (0.2 mL) were collected by piercing the rubber septum stopper with a syringe. The headspace samples were analyzed using GC Clarus 590 series (Perkin Elmer) with a TCD detector. The amount of $H_2$ evolved was calculated based on interpolation from calibration samples of the known $H_2$ concentrations.

*Ex Situ XRD Characterization*: Working electrodes were retrieved from the Swagelok cells after plating and rinsed with HPLC grade water. Glass fiber separators were carefully removed, leaving any pieces that were stuck to the electrode surface in place due to the risk of damaging the Fe mass plated. After vacuum drying, XRD patterns of the electrodes were collected using a Smartlab X-ray Diffractometer (Rigaku) with Ni-filtered Cu Ka radiation at 40 kV and 44 mA.

*In Operando GEIS During Cycling and DRT Analyses*: VMP-3 potentiostat and 3-electrode Swagelok cells with an iron reference electrode were used for GEIS experiments. During the galvanostatic cycling at 1 mA $cm^{-2}$, an AC current of an amplitude of 0.1 mA $cm^{-2}$ was superimposed onto the DC current to collect GEIS data. The frequencies used ranged from 200 kHz to 2 Hz, logarithmically spaced at 20 points per decade. GEIS data were periodically collected every 65 s. The collected GEIS data underwent DRT analysis to visualize the impedance response changes during cycling, using DRTtools MATLAB GUI with a regularization parameter of 0.001 and 2nd-order derivative.[32]

*Femtosecond Stimulated Raman Spectroscopy (FSRS)*: The ground-state (GS) Raman spectra for the electrolytes were collected by a home-built, wavelength-tunable FSRS setup based on a mode-locked Ti:sapphire oscillator and a laser regenerative amplifier (Legend Elite-USP-1K-HE; Coherent, Inc.), providing an ≈800 nm fundamental pulse (FDP) with ≈35 femtoseconds (fs) duration and 1 kHz repetition rate. A detailed description of the spectroscopic setup can be found in the previous publications.[33] In brief, the GS-FSRS setup consists of two ultrafast pulses: a picosecond (ps) Raman pump that is generated by a two-stage ps noncollinear optical parametric amplifier (ps-NOPA), and a fs Raman probe that is supercontinuum white light (SCWL) generated by focusing a small portion of the FDP onto a 2-mm-pathlength quartz cuvette filled with deionized water, followed by temporal compression by a chirped mirror pair (DCM-9, 450–950 nm, Laser Quantum, Inc.). The two incident beams were focused and overlapped on a 1-mm-pathlength cuvette, which houses the electrolyte sample under study. The Raman pump wavelength was tuned to 510 nm for the measurements of all the electrolytes, with typical Raman pump power set to 4–5 mW. The low- and high-frequency spectra were collected with a reflective grating of 1200 and 600 grooves $mm^{-1}$, respectively, to spectrally disperse the probe inside an imaging spectrograph (IsoPlane SCT-320; Princeton Instruments) with a front-illuminated CCD camera (PIXIS:100F) installed at the exit focal plane. All spectra were collected on the Stokes side, i.e., the Raman probe is on the less energetic side of the Raman pump, at room temperature (21 °C) and ambient pressure (1 atm).

*XAS Measurements of Electrolytes*: XAS measurements were done at beamline 4-3 at the Stanford Synchrotron Radiation Lightsource, SLAC National Accelerator Laboratory. The electrolytes were filled in the polyimide tubes with 0.8 mm thickness for data collection. The XAS measurements were carried out in the fluorescence mode and collected at the Fe K-edge (7112 eV) using a Lytle detector. Fe metal foil was used as the reference for X-ray energy calibration and data alignment. XANES data processing and $f_{eff}$ analysis were performed on Athena and Artemis software from the Demeter package. The imaginary part of the complex $\chi(R)$ was calculated from EXAFS by taking the Fourier Transform of weighted $k^3$ $\chi(k)$ along with the magnitude of the Fourier Transform using the formula below

$$\chi(k) = \frac{NS_0^2 F(K)}{2kR} \sin(2kR + \delta(k)) \, e^{-2\sigma^2 k^2} \tag{1}$$

*Ex Situ Surface Characterization*: Beaker cells without separators were used to prepare working electrode samples for ex situ surface characterization. Ti current collectors, after the plating step, were rinsed with HPLC grade water and vacuum dried before transfer to the sample holder. SEM and EDS mapping were carried out on the SU8020 field-emission scanning electron microscopy (Hitachi). XPS was performed with VersaProbe 4 XPS (Physical Electronics, Inc.) with monochromatized Al(Ka) radiation, and a charge neutralizer was applied to compensate for the sample surface charge. The measurement parameters were set to 200 µm spot size, 50 W power, and 15 kV X-ray voltage. During XPS measurements, a 50 ms time step was employed, with a pass energy of 112 eV. Depth profiling was conducted under consistent $Ar^+$ sputtering conditions. To avoid the contamination and oxidation of the sample in the air, the XPS transfer vessel was applied during the transfer process. All binding energies were calibrated to C1s peak at 284.8 eV.

## Supporting Information

Supporting Information is available from the Wiley Online Library or from the author.

## Acknowledgements

M.S.J., and S.Y. contributed equally to this work. This work was supported by the Aqueous Battery Consortium, an energy innovation hub under the U.S. Department of Energy, Office of Basic Energy Sciences, Division of Materials Science and Engineering. This work was also supported by the U.S. National Science Foundation (NSF) with Award Nos. DMR-2221645 and CBET-2038381. Part of this work was performed at the Stanford Nano Shared Facilities RRID:SCR_023230, supported by the National Science Foundation under Award No. ECCS-2026822.

## Conflict of Interest

The authors declare no conflict of interest.

## Data Availability Statement

The data that support the findings of this study are available in the supplementary material of this article.

## Keywords

aqueous electrolytes, ion speciation, iron ion batteries, iron metal anode, solid electrolyte interphase

Received: December 14, 2024
Revised: February 14, 2025
Published online: March 18, 2025

[1] C. Chakkaravarthy, P. Periasamy, S. Jegannathan, K. I. Vasu, *J. Power Sources* **1991**, *35*, 21.

[2] a) Y. Zeng, Q. Liu, J. Zhang, H. You, H. Mo, D. Yan, *Energy Fuels* **2024**, *38*, 17309; b) D. Chao, W. Zhou, F. Xie, C. Ye, H. Li, M. Jaroniec, S.-Z. Qiao, *Sci. Adv.* **2020**, *6*, eaba4098.

[3] a) X. Wu, A. Markir, Y. Xu, C. Zhang, D. P. Leonard, W. Shin, X. Ji, *Adv. Funct. Mater.* **2019**, *29*, 1900911; b) S. Yu, X. Yue, J. Holoubek, X. Xing, E. Pan, T. Pascal, P. Liu, *J. Power Sources* **2021**, *513*, 230457; c) S. Belongia, X. Wang, X. Zhang, *Adv. Funct. Mater.* **2024**, *34*, 2302077; d) C. Bai, H. Jin, Z. Gong, X. Liu, Z. Yuan, *Energy Storage Mater.* **2020**, *28*, 247.

[4] X. Wu, H. Zhang, K.-J. Huang, Z. Chen, *Nano Lett.* **2020**, *20*, 1700.

[5] a) C. Li, A. Shyamsunder, A. G. Hoane, D. M. Long, C. Y. Kwok, P. G. Kotula, K. R. Zavadil, A. A. Gewirth, L. F. Nazar, *Joule* **2022**, *6*, 1103; b) Y. Jin, K. S. Han, Y. Shao, M. L. Sushko, J. Xiao, H. Pan, J. Liu, *Adv. Funct. Mater.* **2020**, *30*, 2003932; c) F. Wang, O. Borodin, T. Gao, X. Fan, W. Sun, F. Han, A. Faraone, J. A. Dura, K. Xu, C. Wang, *Nat. Mater.* **2018**, *17*, 543. d) F. Wang, J. Zhang, H. Lu, H. Zhu, Z. Chen, L. Wang, J. Yu, C. You, W. Li, J. Song, Z. Weng, C. Yang, Q.-H. Yang, *Nat. Commun.* **2023**, *14*, 4211.

[6] a) K. L. Hawthorne, T. J. Petek, M. A. Miller, J. S. Wainright, R. F. Savinell, *J. Electrochem. Soc.* **2015**, *162*, A108; b) Y. Song, H. Yan, H. Hao, Z. Liu, C. Yan, A. Tang, *Small* **2022**, *18*, 2204356; c) B. S. Jayathilake, E. J. Plichta, M. A. Hendrickson, S. R. Narayanan, *J. Electrochem. Soc.* **2018**, *165*, A1630.

[7] J. Liu, D. Dong, A. L. Caro, N. S. Andreas, Z. Li, Y. Qin, D. Bedrov, T. Gao, *ACS Cent. Sci.* **2022**, *8*, 729.

[8] P. Bai, J. Li, F. R. Brushett, M. Z. Bazant, *Energy Environ. Sci.* **2016**, *9*, 3221.

[9] H. Jiang, L. Tang, Y. Fu, S. Wang, S. K. Sandstrom, A. M. Scida, G. Li, D. Hoang, J. J. Hong, N.-C. Chiu, K. C. Stylianou, W. F. Stickle, D. Wang, J. Li, P. A. Greaney, C. Fang, X. Ji, *Nat. Sustainable.* **2023**, *6*, 806.

[10] a) A. Jain, S. P. Ong, G. Hautier, W. Chen, W. D. Richards, S. Dacek, S. Cholia, D. Gunter, D. Skinner, G. Ceder, K. A. Persson, *APL Mater.* **2013**, *1*, 011002; b) A. K. Singh, L. Zhou, A. Shinde, S. K. Suram, J. H. Montoya, D. Winston, J. M. Gregoire, K. A. Persson, *Chem. Mater.* **2017**, *29*, 10159; c) A. M. Patel, J. K. Nørskov, K. A. Persson, J. H. Montoya, *Phys. Chem. Chem. Phys.* **2019**, *21*, 25323; d) K. A. Persson, B. Waldwick, P. Lazic, G. Ceder, *Phys. Rev. B* **2012**, *85*, 235438.

[11] B. Beverskog, I. Puigdomenech, *Corros. Sci.* **1996**, *38*, 2121.

[12] F. A. Schimmel, *J. Am. Chem. Soc.* **1952**, *74*, 4689.

[13] W. Wu, X. Yang, K. Wang, C. Li, X. Zhang, H.-Y. Shi, X.-X. Liu, X. Sun, *Chem. Eng. J.* **2022**, *432*, 134389.

[14] H. Kanno, J. Hiraishi, *J. Raman Spectrosc.* **1982**, *12*, 224.

[15] U. Luin, I. Arčon, M. Valant, *Molecules* **2022**, *27*, 642.

[16] a) S. L. Altmann, P. Herzig, *Point-Group Theory Tables*, Clarendon Press, Oxford **1994**; b) R. L. Carter, *J. Chem. Educ.* **1991**, *68*, 373.

[17] a) D. E. Irish, B. McCarroll, T. F. Young, *J. Chem. Phys.* **1963**, *39*, 3436; b) C. Zhang, J. Holoubek, X. Wu, A. Daniyar, L. Zhu, C. Chen, D. P. Leonard, I. A. Rodríguez-Pérez, J.-X. Jiang, C. Fang, X. Ji, *Chem. Commun.* **2018**, *54*, 14097.

[18] a) L. Tang, Y. Xu, W. Zhang, Y. Sui, A. Scida, S. R. Tachibana, M. Garaga, S. K. Sandstrom, N.-C. Chiu, K. C. Stylianou, S. G. Greenbaum, P. A. Greaney, C. Fang, X. Ji, *Angew. Chem., Int. Ed.* **2023**, *62*, 202307212; b) C. Zhang, W. Shin, L. Zhu, C. Chen, J. C. Neuefeind, Y. Xu, S. I. Allec, C. Liu, Z. Wei, A. Daniyar, J.-X. Jiang, C. Fang, P. Alex Greaney, X. Ji, *Carbon Energy* **2021**, *3*, 339; c) Q. Sun, *Chem. Phys. Lett.* **2013**, *568–569*, 90.

[19] H. Hwang, Y. C. Cho, S. Lee, Y.-H. Lee, S. Kim, Y. Kim, W. Jo, P. Duchstein, D. Zahn, G. W. Lee, *Chem. Sci.* **2021**, *12*, 179.

[20] B. Ravel, M. Newville, *J. Synchrotron. Radiat.* **2005**, *12*, 537.

[21] I. Persson, *J. Solution Chem.* **2018**, *47*, 797.

[22] a) G. Zhang, X. Zhang, H. Liu, J. Li, Y. Chen, H. Duan, *Adv. Energy Mater.* **2021**, *11*, 2003927; b) Y. Zeng, X. Zhang, R. Qin, X. Liu, P. Fang, D. Zheng, Y. Tong, X. Lu, *Adv. Mater.* **2019**, *31*, 1903675.

[23] Á. Révész, T. Ungár, A. Borbély, J. Lendvai, *Nanostruct. Mater.* **1996**, *7*, 779.

[24] T. Takayama, S. Shinohara, K. Ishida, T. Nishizawa, *J. Phase Equilib.* **1995**, *16*, 390.

[25] C. Li, R. Kingsbury, A. S. Thind, A. Shyamsunder, T. T. Fister, R. F. Klie, K. A. Persson, L. F. Nazar, *Nat. Commun.* **2023**, *14*, 3067.

[26] T.-C. Lin, G. Seshadri, J. A. Kelber, *Appl. Surf. Sci.* **1997**, *119*, 83.

[27] A. P. Grosvenor, B. A. Kobe, M. C. Biesinger, N. S. McIntyre, *Surf. Interface Anal.* **2004**, *36*, 1564.

[28] a) S. Wang, G. Liu, W. Wan, X. Li, J. Li, C. Wang, *Adv. Mater.* **2024**, *36*, 2306546; b) G. Li, W. Chen, H. Zhang, Y. Gong, F. Shi, J. Wang, R. Zhang, G. Chen, Y. Jin, T. Wu, Z. Tang, Y. Cui, *Adv. Energy Mater.* **2020**, *10*, 1902085.

[29] Z. Li, Y. Ren, L. Mo, C. Liu, K. Hsu, Y. Ding, X. Zhang, X. Li, L. Hu, D. Ji, G. Cao, *ACS Nano* **2020**, *14*, 5581.

[30] C. Spanos, D. E. Turney, V. Fthenakis, *Renewable Sustainable Energy Rev.* **2015**, *43*, 478.

[31] M. S. Jung, D. Hoang, Y. Sui, X. Ji, *ACS Energy Lett.* **2024**, *9*, 4316.

[32] T. H. Wan, M. Saccoccio, C. Chen, F. Ciucci, *Electrochim. Acta* **2015**, *184*, 483.

[33] a) L. Zhu, W. Liu, C. Fang, *Appl. Phys. Lett.* **2014**, *105*, 041106; b) C. Chen, H. Zhang, J. Zhang, H.-w. Ai, C. Fang, *Phys. Chem. Chem. Phys.* **2023**, *25*, 15624; c) Y. Sui, A. M. Scida, B. Li, C. Chen, Y. Fu, Y. Fang, P. A. Greaney, T. M. Osborn Popp, D. Jiang, C. Fang, X. Ji, *Angew. Chem., Int. Ed.* **2024**, *63*, 202401555.